Fano resonance in atomic-resolution spectroscopic imaging of solids

C. Dwyer, H. L. Xin, and D. A. Muller

Fano resonance in atomic-resolution spectroscopic imaging of solids

C. Dwyer,[1, *] H. L. Xin,[2] and D. A. Muller[3]

[1] *Monash Centre for Electron Microscopy & Department of Materials Engineering & ARC Centre of Excellence for Design in Light Metals, Monash University, Victoria 3800, Australia*
[2] *Department of Physics, Cornell University, Ithaca, NY 14853*
[3] *School of Applied and Engineering Physics & Kavli Institute, Cornell University, Ithaca, NY 14853*

We report direct evidence of Fano resonances in atomic-resolution imaging of a crystalline material using a focused electron beam. Spectroscopic images of $DyScO_3$ that are derived from the Fano resonance in the Dy-$N_{4,5}$ spectrum can exhibit unexpected atomic-scale contrast, markedly different to non-resonant images. These effects are explained by our theoretical calculations of the inelastic and elastic scattering, and show excellent agreement with the experimental data. The results have significant implications for spectroscopic imaging of rare-earth elements at the atomic scale.

INTRODUCTION

Fano resonance is an intriguing phenomenon in spectroscopy that arises when an atom has a discrete excited state that resides within a continuum portion of its energy spectrum [1–4]. Upon excitation, resonance occurs as a manifestation of interactions within the atom that cause transitions between the discrete and continuum states, eventually resulting in autoionization of the atom. In archetypal experiments, the effect is often observed as a characteristically-asymmetric peak – a Beutler-Fano profile – in the atom's absorption or emission spectrum. Here we report the observation of effects associated with Fano resonances in atomically-resolved spectroscopic images of a crystalline material generated using a focused electron beam. Spectroscopic images generated from the Dy-$N_{4,5}$ spectra of crystalline $DyScO_3$ exhibit unexpected effects which reflect changes in the spatial distribution of the excited atomic wave functions. The effects are in excellent agreement with our calculations, and have important consequences for the interpretation of spectroscopic imaging of rare-earth elements at the atomic scale.

Atomic-resolution spectroscopic imaging is a recent development in the characterization of nanomaterials. These experiments use an aberration-corrected [5] scanning transmission electron microscope (STEM) to scan a fine, atomic-sized beam of high-energy electrons across an electron-transparent sample. A spectrometer is synchronized to record the transmitted electron energy-loss spectrum for each position of the beam, resulting in three-dimensional data set (beam position x, y and energy loss ΔE) known as a spectrum image. In principal applications of the technique, chemical edges in the spectra are utilized to extract atomic-scale maps of the sample's chemical composition and electronic bonding [6–13].

For chemical mapping of rare-earth elements, the $N_{4,5}$ spectra are important for several reasons. Firstly,
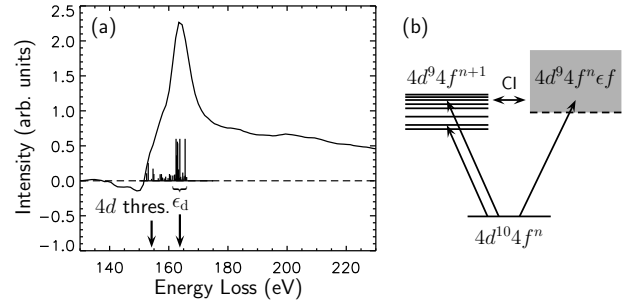

FIG. 1: (a) Dy-$N_{4,5}$ electron energy-loss spectrum exhibiting Fano resonance. Computed relative photoabsorption oscillator strengths for transitions to $4d^9 4f^{n+1}$ are overlaid for comparison, ϵ_d denoting the average upper energy of strong transitions. (b) Corresponding energy level structure (schematic) with arrows indicating transitions (CI stands for 'configuration interaction').

obtaining an adequate signal-to-noise ratio is often challenging. The rare-earth $N_{4,5}$ edges lie at relatively low energies (100–180 eV), and hence their strong signal can be used to provide atomic-resolution maps of high-quality. Secondly, these edges lie above the vast majority of low-energy excitations, and so are reasonably placed for a reliable subtraction of the background signal. Thirdly, the collapse of the $4f$ orbitals in the rare-earths implies that the near-threshold signal is relatively insensitive to the solid-state environment of the rare-earth element, offering the possibility of quantifying the rare-earth concentration in a wide range of materials [14].

Fig. 1 shows a Dy-$N_{4,5}$ electron energy-loss spectrum from $DyScO_3$ (a proposed high-k dielectric material [15]). This spectrum represents transitions from the $4d$ subshell, and, like the vast majority of rare-earth $N_{4,5}$ spectra, exhibits a strong resonance at several electron volts above the $4d$ threshold [2–4]. The energy level structure of the excited Dy configuration $4d^9 4f^{n+1}$ is strongly split due to the exchange interaction between the $4d$ hole and the partially-filled $4f$

subshell, pushing some $4d^9 4f^{n+1}$ discrete levels well above the $4d$ ionization threshold and into the continuum. Upon excitation, the configuration interaction between these discrete levels and the $4d^9 4f^n \epsilon l$ continuum levels gives rise to resonance [16]. Following Fano [1, 17, 18], the situation can be pictured in terms of exciting 'new' atomic states that are a superposition of the discrete and continuum states:

$$|\alpha, \epsilon\rangle = c_{\rm d}(\epsilon)|\alpha_{\rm d}\rangle + c_{\rm c}(\epsilon)|\alpha_{\rm c}, \epsilon\rangle, \qquad (1)$$

where ϵ denotes energy and the α's are shorthand for the quantum numbers necessary to specify the states. The coefficients $c_{\rm d}(\epsilon)$ and $c_{\rm c}(\epsilon)$ are functions of the energy ϵ, and are given by the expressions

$$c_{\rm d}(\epsilon) = \frac{1}{\pi v (\eta^2 + 1)^{1/2}}, \qquad c_{\rm c}(\epsilon) = \frac{\eta}{(\eta^2 + 1)^{1/2}}, \quad (2)$$

where v represents the strength of the configuration interaction, and $\eta = (\epsilon - \epsilon_{\rm d})/\pi v^2$ is the energy relative to the discrete state's energy $\epsilon_{\rm d}$ [19]. The form of $c_{\rm d}(\epsilon)$ implies that the discrete contribution is significant for energies within about πv^2 of $\epsilon_{\rm d}$. Within this regime, if $\epsilon < \epsilon_{\rm d}$, then the coefficients $c_{\rm d}(\epsilon)$ and $c_{\rm c}(\epsilon)$ have opposite signs, implying destructive interference of the discrete and continuum states; if $\epsilon > \epsilon_{\rm d}$, then constructive interference occurs, giving rise to a peak in the spectrum, i.e. the large peak in Fig. 1a. For energies well above $\epsilon_{\rm d}$, the discrete contribution tends to zero and the spectrum is smooth, reflecting the slowly-varying nature of the continuum states with increasing energy.

In the present work, we report the affect of the Dy-$N_{4,5}$ resonance on atomic-resolution spectroscopic imaging of $DyScO_3$.

EXPERIMENTAL

Experiments were performed using an aberration-corrected Nion UltraSTEM operating at 100 kV, with a probe convergence semi-angle of 32 mrad. Spectrum images were recorded using a Gatan Enfina spectrometer with an 80 mrad collection semi-angle, energy dispersion of 1.1 eV/channel, and a dwell time of 10 msec/pixel. For this energy dispersion, the energy resolution of the instrument can be taken as 2.2 eV, which is slightly greater than the actual resolution of 2.0 eV (see Fig. 2), and is comfortably adequate for our investigation of the Dy-$N_{4,5}$ resonance.

Sample-drift correction based on corrective geometric transformations was applied to the raw spectrum images. For a given spectrum image data set, the required geometric transformation was obtained by applying a cross-correlation technique to the crystal lattice in simultaneously acquired high-angle an-

nular dark-field (ADF) image (details on the cross-correlation technique can be found in Refs. [20, 21]); the geometric transformation so obtained was then applied to each image in the spectrum image data set. After power-law background extrapolation and subtraction, Dy-$N_{4,5}$ spectroscopic images were extracted using 10 eV energy integration windows at the resonance peak, and between 10 and 20 eV windows at the higher energies. The processed experimental images were obtained by averaging the drift-corrected spectroscopic images over 10–15 unit cells and then applying low-pass Fourier filtering at a resolution of 80 pm, which improves the noise while preserving the resolution of the data as determined by the instrument's effective source distribution (see below). In results presented below, the drift-corrected averages are repeated in a 2×2 format to emphasize the periodicity of the structure and for ease of viewing. Examples of the data processing are shown in Fig. 3.

The sample thicknesses were measured using the intensities obtained from quantitatively-recorded position-averaged incoherent bright-field images [22].

ADF images were acquired simultaneously with the spectra using an ADF detector with semi-angles 98 to 295 mrad. The ADF images were used to determine the electron probe's position on the sample, as well as infer the reduction in image contrast arising from source size effects. The effective source distribution was modeled as a 71 pm FWHM Gaussian convoluted with a 18 pm FWHM truncated Lorentzian, the parameters of which were determined by quantitative matching of the experimental ADF image contrast with frozen-phonon multislice simulations [23, 24] over a large range (20 to 90 nm) of specimen thicknesses (see Refs. [25, 26] for related work).
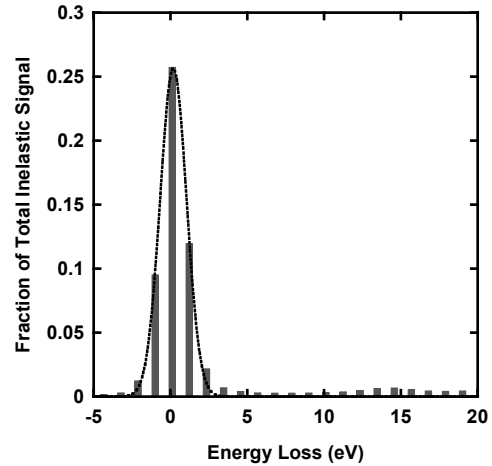

FIG. 2: Measurement of spectrometer energy resolution. A Gaussian fit to the zero-loss peak in the energy-loss spectrum gives a resolution of 2.0 eV (defined by the full-width at half-maximum).
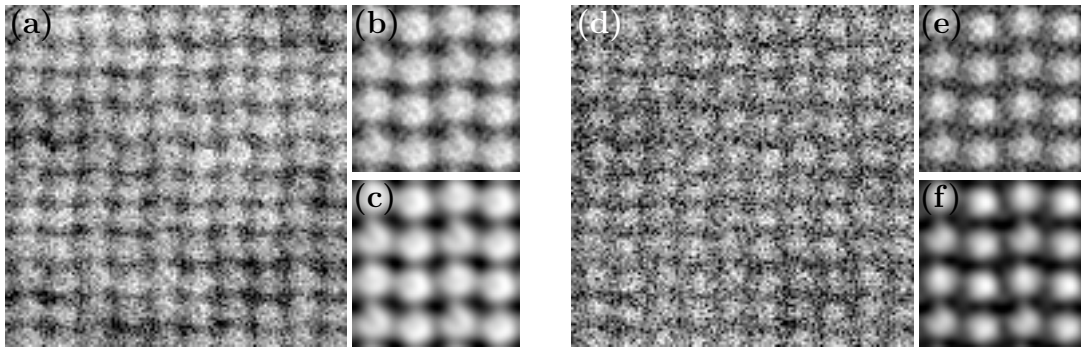
FIG. 3: Processing of experimental data. a, Raw spectroscopic image extracted from a 10 eV window centered on the Dy-$N_{4,5}$ resonance peak for the 21 nm-thick DyScO$_3$ sample; b, Unit-cell averaging applied to the image in a (after sample-drift correction) and repeated in a 2×2 format; c, low-pass filtering applied to the image in b; d–f, Analogous images from a 20 eV window centered at 80 eV above the Dy-$N_{4,5}$ resonance.

The background-subtracted spectrum shown in Fig. 1 is the result of position-averaging over 4 of the spectrum images described above, which were acquired from specimen areas of similar thicknesses (21 to 24 nm).

THEORETICAL

A convenient theoretical formulation of the relevant scattering physics is provided by the following expression for the wave function of an inelastically-scattered high-energy electron at the specimen's exit surface [27–29]:

$$
\psi_\alpha(\mathbf{x}, \mathbf{x}_0) = \int \mathrm{d}^2\mathbf{x}'' \, iG_\alpha(\mathbf{x}t, \mathbf{x}''z)(-i\sigma_\alpha)V_\alpha(\mathbf{x}'')
$$
$$
\times \int \mathrm{d}^2\mathbf{x}' \, iG_0(\mathbf{x}''z, \mathbf{x}'0)\psi_0(\mathbf{x}' - \mathbf{x}_0) \, .
$$
$$(3)$$

Here bold symbols denote two-dimensional vectors transverse to the optic axis, t is the sample thickness, ψ_0 is the electron beam's wave function at the entrance surface, $\mathbf{x}_0$ is the beam position on the entrance surface, V_α is a (projected, or z-integrated) transition potential associated with exciting a given atom from its ground state to a state $|\alpha\rangle$, z is the depth of the inelastic event in the specimen, and the Green functions G_0 and G_α describe elastic scattering before and after the excitation event, respectively. The simulation of atomic-resolution spectroscopic images involves computing the intensity of inelastically-scattered electrons on a detector in the far-field, as a function of the beam position $\mathbf{x}_0$. Spectroscopic images contain contributions from all atoms of a given type, and, for each atom, contributions from many excited states.

Simulations of spectroscopic images were performed using a multislice-based theory of atomic inner-shell excitation [27, 28], executed on a GPGPU-based cluster. The simulations used supercells of size 3.2 nm $\times$ 3.2 nm (4×4 projected unit cells of [101] DyScO$_3$), sampling using 512×512 pixels. The simulations assumed an aberration-free electron probe. Source size effects were incorporated into the simulations by convolution with the source distribution determined by fitting to the experimental ADF images (see previous section). Thermal diffuse scattering was included via the frozen-phonon algorithm [23, 24], using vibration parameters taken from the literature [30]. The simulations take into account multiple elastic and thermal diffuse scattering before and after a given atomic excitation event. Multiple atomic excitations are safely ignored on account of the small cross-sections. Plasmon scattering has not been included. While plasmon excitations become highly probable in the thicker samples, the dependence of such excitations on the high-energy electron's position within the unit cell is weak, and hence its influence on the qualitative appearance of spectroscopic images is not very important.

Projected transition potentials were computed based on the theory described in [27, 28], using radial atomic wave functions obtained from the Cowan code [17]. A single-electron-hole-pair description of the resonance [18] was used, which omits effects associated with the partially-filled outer shells, i.e. the $4f$ shell the present case. In this description, the ground configuration is effectively modeled as $4d^{10}$, the excited discrete and continuum configurations are modeled as $4d^9 4f$, and $4d^9 \epsilon l$, respectively, where for the continuum we included $l = s, d, f$.

The calculations presented below include the configuration interaction between the discrete and continuum $d^9 f$ configurations [4]. Due to the relatively small scattering angles experienced by high-energy electrons in a TEM, spin-flips can be ignored, so that the rel-

evant atomic levels are the singlets $d^9f\,^1P$ through $d^9f\,^1H$. Among these levels, only the dipole-allowed transitions to ^1P levels are appreciable (even though we did not invoke the dipole approximation). These transitions involve a change in the total orbital angular momentum of $\Delta L = +1$, and are referred to as "P-type" transitions. Among these P-type transitions, those for $\Delta M = \pm 1$ tend to dominate. While the contributions depend on the specific position of the electron beam and the energy loss, some idea is gained from calculations assuming a 100 keV incident plane wave: for transitions $4d^{10} \rightarrow 4d^9 4f$, the contributions of the P-type transitions with $\Delta M = -1, 0, +1$ are 42.8%, 13.8%, 42.8%, respectively, with the remaining 0.6% contained in the dipole-forbidden non-P-type transitions.

Based on the simplified theory outlined in Ref. [18], and using radial wave functions from the Cowan code, the strength of the configuration interaction between ^1P levels was calculated to be $v \approx +1.4$ eV$^{1/2}$, and approximately constant over the relevant energy range. This value of v corresponds to a resonance peak width of about 13 eV, in good agreement with the experimentally observed width in Fig. 1. The approximate constancy of v implies the validity of the simplified superposition of discrete and continuum states outlined above (see Ref. [17] for further discussion).

The relative photoabsorption oscillator strengths shown in Fig. 1 were calculated using the Cowan code with the scaling of radial integrals quoted in Ref. [3].

RESULTS AND DISCUSSION

Fig. 4 shows processed experimental atomic-resolution spectroscopic images of DyScO$_3$ extracted from the resonance peak in the Dy $N_{4,5}$ spectrum, as well as images extracted at energies well above the resonance peak. For each energy, images are presented for a range of thicknesses of the DyScO$_3$ sample. Also shown in Fig. 4 are the corresponding simulations based on the theory described above. Images extracted from the resonance peak exhibit significant differences from those extracted at higher energies: In a very thin sample (10 nm), the Dy atomic columns appear significantly broader in the resonance images; as the sample thickness increases (21, 28 and 45 nm), the Dy columns appear broader still, and minima develop at the Dy sites themselves, so that each Dy column appears as a ring-shaped feature; this behavior continues until, in the thickest samples (60 and 71 nm), the intensity is spread throughout the unit cell except for the strong minima located on and between the Dy columns. This behavior implies that, in all but the thinnest samples, the strong signal at the res-

onance does not give rise to images that can be directly interpreted in terms of the atom locations. In contrast to this behavior, the non-resonant images exhibit much weaker minima and the intensity remains substantially localized on the Dy columns, especially for energies well above the resonance.

While minima similar to those seen in the resonance images have been observed in the past [7, 29, 31–37], those observations could be attributable to coherent effects arising from the use of a collection angle comparable or smaller than the probe convergence angle. In the present work, we use a large collection angle (80 mrad), where the incoherent nature of scattering and detection means that such minima are unexpected. Moreover, strong minima are not present in the non-resonant Dy-$N_{4,5}$ images (Fig. 4) or the Dy-M_5 images (Fig. 5) extracted from the same data sets. In addition, the sensitive dependence of the spectroscopic images on the energy, as seen in Fig. 4, is unusual and has not been published previously.

For the purposes of comparison, Fig. 5 shows processed experimental and simulated Dy-M_5 spectroscopic images of [110] DyScO$_3$. These experimental images were extracted from the same data sets as used for Fig. 4, and therefore correspond to precisely the same experimental conditions. The simulations in Fig. 5 show good agreement with the experimental data. As stated above, the Dy-M_5 images do not exhibit minima at the sites of Dy (for all sample thickness considered here).

Initially, the larger degree of spreading in the resonance images in Fig. 4 might seem perplexing: The resonance peak in the Dy-$N_{4,5}$ spectrum contains a large contribution from the $4d^9 4f^{n+1}$ discrete levels, while well above the resonance peak the $4d^9 4f^n \epsilon l$ continuum levels dominate. Since the ϵl continuum wave functions extend to much larger (in principle, infinite) radii than the $4f$ wave functions, we might well expect the resonance images to exhibit *less* spreading, contrary to Fig. 4. However, as shown below, the spreading of intensity in the resonance images can be understood in terms of the transition potentials for the relevant transitions.

The spatial variation of the transition potentials (TPs) is pertinent to an understanding of the present results. In the case of resonance, the transition potentials are a superposition of those for transitions to the discrete and continuum states [see Eq. (1)]:

$$V_{\alpha,\epsilon}(\mathbf{x}) = c_{\mathrm{d}}(\epsilon)V_{\alpha_{\mathrm{d}}}(\mathbf{x}) + c_{\mathrm{c}}(\epsilon)V_{\alpha_{\mathrm{c}},\epsilon}(\mathbf{x}). \qquad (4)$$

Fig. 6 shows ψ_0, along with the discrete TPs (DTPs) $V_{\alpha_{\mathrm{d}}}$ and continuum TPs (CTPs) $V_{\alpha_{\mathrm{c}},\epsilon}$ relevant to the Dy-$N_{4,5}$ resonance. The amplitudes of the DTPs have been scaled to match the CTPs at positions away from the atomic nucleus, which serves to highlight their different spatial variations more clearly. Essentially,
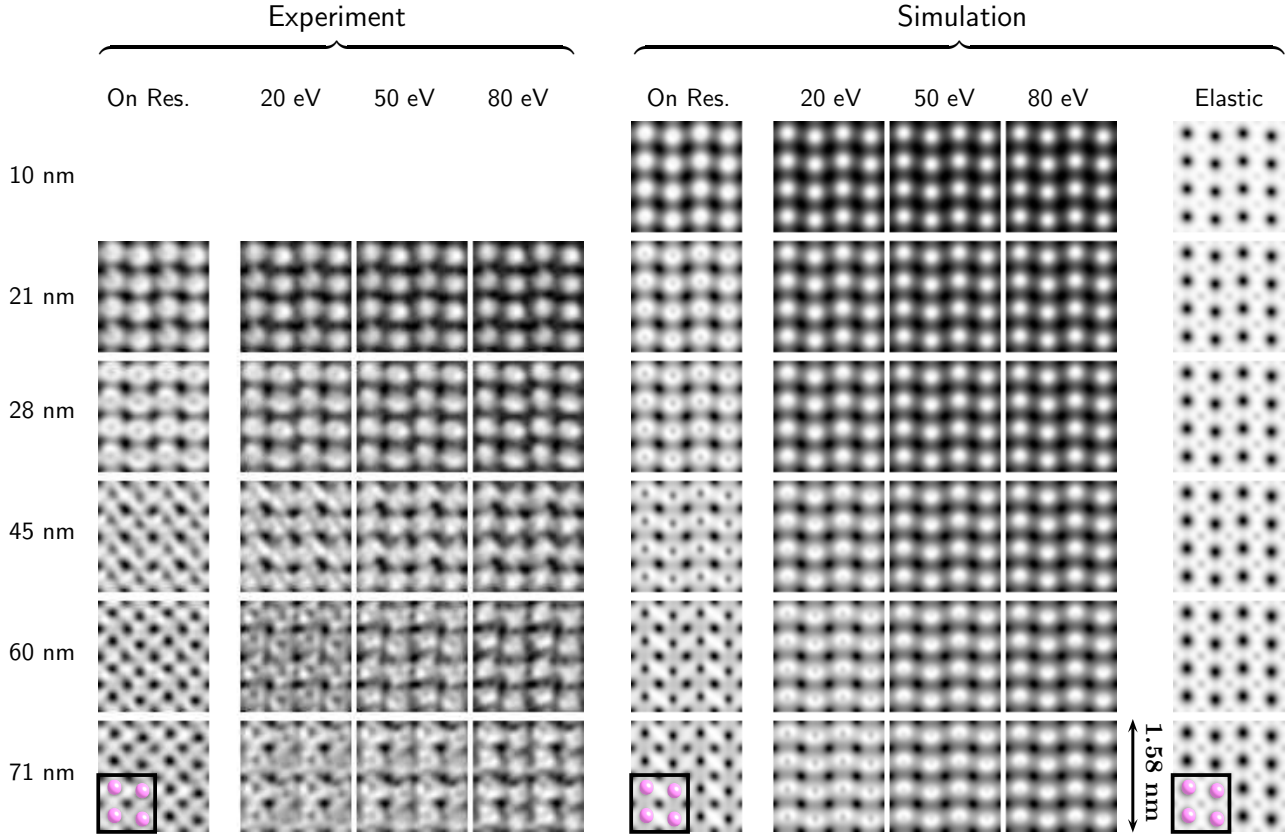
FIG. 4: Fano resonance in Dy-$N_{4,5}$ atomic-resolution spectroscopic imaging of [101] DyScO$_3$. Processed experimental and simulated spectroscopic images are shown for different energies (indicated atop) and sample thicknesses (indicated at left). "On Res." refers to the resonance peak, while indicated energies are relative to the peak. Simulations of images generated by elastic scattering are shown for comparison. Atomic models indicating the Dy sites in a single unit cell are overlaid (for clarity the models omit Sc and O). For ease of viewing, the processed experimental images consist of data for one projected DyScO$_3$ unit cell which is replicated to cover the area of 2×2 unit cells.

the DTPs vary quite smoothly, which can be traced back to the closely matched forms of the $4d$ and $4f$ radial wave functions involved in the discrete transitions. The CTPs, on the other hand, feature a much more pronounced peak on or near the nucleus (which occurs for all relevant energies ϵ).

Regarding Fig. 4, it is the comparative smoothness of the DTPs that causes the broader appearance of Dy columns in the resonance images of thinner samples. To understand the results in thicker samples, we must also consider the elastic scattering that inevitably occurs before (and after) each excitation event. When the electron beam is positioned directly over a Dy atomic column (solid curve in Fig 6a), the heavy Dy atoms cause the beam to be strongly elastically scattered to high angles as it progresses through the sample, reducing the prospect of generating a spectroscopic signal. On moving the beam to a position immediately adjacent to a Dy column (dashed curve in Fig 6a), elastic scattering is reduced and the prospect of generating a signal increases (see the elastic images in Fig. 4). In the case of resonance images, because the DTPs retain comparable values as the beam moves away from the Dy column, the net effect can be an *increase* in the signal. Put another way, the comparative smoothness of the DTPs leads to an approximate 'preservation of elastic contrast' [38] in the resonance images of thicker samples (compare the resonance and elastic images in Fig. 4). Well above resonance, the pronounced peaks in the CTPs on or near the nuclei tend to compensate for this effect, so that the spectroscopic signal remains substantially localized on the Dy columns.

The size of the collection angle is an important parameter in regard to the appearance of atomic-resolution spectroscopic images. For a collection semi-angle β smaller than the probe convergence semi-angle (here 32 mrad), coherent effects can dominate the appearance of the spectroscopic images, making them non-intuitive to interpret. (An atomic-resolution spectroscopic image is amenable to an intuitive interpretation if it consists of intensity max-
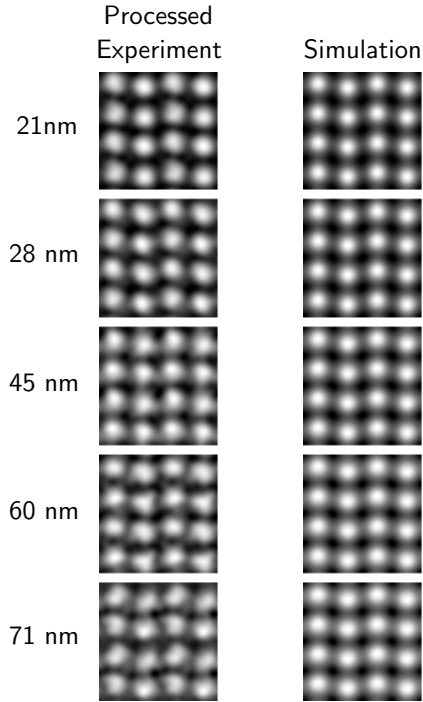
FIG. 5: Dy-M_5 spectroscopic images of [110] DyScO$_3$. Processed experimental and simulated spectroscopic images as a function of sample thickness. The spatial scale, etc., are identical to those in Fig. 4.
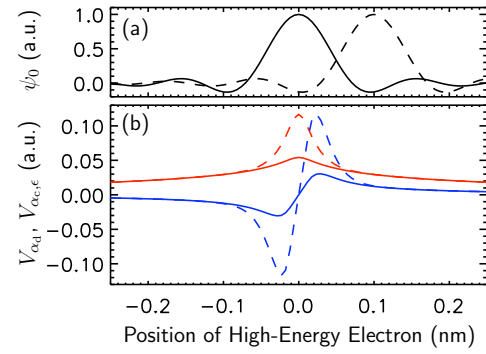

FIG. 6: (a) Electron wave function's for two beam positions on entrance surface, calculated using parameters matching experiment. (b) Line traces through the centers of transition potentials for P-type transitions to discrete (solid) and 10 eV continuum (dashed) states associated with Dy-$N_{4,5}$ resonance. Red and blue curves refer, respectively, to transitions involving changes of 0 and +1 in the magnetic quantum number M (for $\Delta M = +1$ only the real part is shown). The atomic nucleus is located at the abscissa origin.

ima located at the positions of the atomic species in question.) Hence the collection angle should be as large as possible without sacrificing the required energy resolution, as determined by the aberrations of the post-specimen lenses and spectrometer. In our experiments, we used $\beta = 80$ mrad, which is considerably larger than the probe convergence semi-angle, in order to avoid coherent effects. Even with such a large collection angle, however, the Dy-$N_{4,5}$ resonance images of [110] DyScO$_3$ exhibit non-intuitive atomic-scale contrast due the slowly varying transition potentials and, in thicker samples, elastic scattering (as discussed above). In Fig. 7, we present simulations of spectroscopic images, at energies both on resonance and at 50 eV above resonance, as a function of β and sample thickness. It is seen that at 50 eV above resonance the image contrast is essentially intuitive for all collection angles and thickness considered here. On the other hand, when β is increased from 80 mrad to 130 mrad, the resonance images of thinner samples become intuitive, but those of thicker samples still exhibit ring-like features located at the Dy atomic columns (similar to the ring-like features encountered in thinner samples when $\beta = 80$ mrad). Only when β is increased to 180 mrad are the effects of elastic scattering on the qualitative appearance of the reso-

nance images circumvented in the thickest samples, so that the resonance images become essentially intuitive across all thicknesses considered here. Nonetheless, even for this *extremely* large collection angle, differences between the resonance images and non-resonant images (those at 50 eV) persist, in the form of the broader appearance of the atomic columns in the resonance images.

Before concluding, we examine more closely the spectroscopic images extracted from the resonance peak in the Dy-$N_{4,5}$ spectrum. We anticipate that images extracted from the left and right portions of the resonance peak should exhibit differences associated with the change from destructive to constructive interference mentioned in the introduction. The results are shown in Fig. 8, where we do indeed observe discernible changes in images extracted from 5 eV windows centered at ± 2.5 eV relative to the peak maximum. In particular, the images at -2.5 eV exhibit stronger minima at the Dy sites, while those at $+2.5$ eV exhibit stronger minima *between* the Dy sites. These trends, for which the simulated and experimental images show good agreement, can be rationalized in terms of adding the discrete and continuum contributions with the appropriate phases.

CONCLUSION

In summary, we have presented direct evidence of Fano resonances atomic-resolution spectroscopic imaging with high-energy electrons. In the thinnest DyScO$_3$ samples studied here, the slower spatial vari-
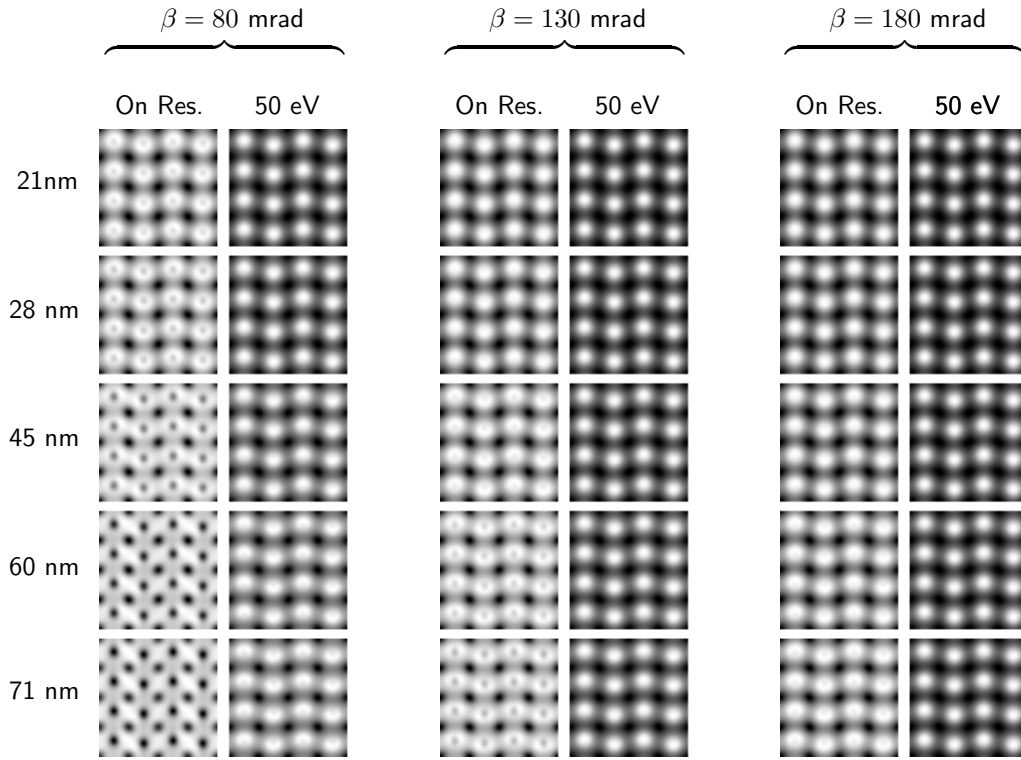
FIG. 7: Simulated Dy-$N_{4,5}$ spectroscopic images of [110] DyScO$_3$. Images at energies both on resonance images and at 50 eV above the resonance are shown as a function of collection semi-angle β (indicated atop) and sample thickness (indicated at left). The spatial scale, etc., are identical to those in Fig. 4.
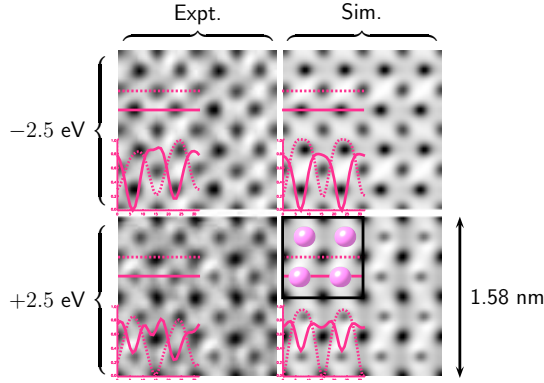

FIG. 8: Processed experimental and simulated Dy-$N_{4,5}$ spectroscopic images of DyScO$_3$ extracted at ± 2.5 eV relative to the resonance peak. Line traces across (solid) and between (dashed) Dy sites are overlaid. The sample thickness is 60 nm.

than the probe convergence angle is used. In contrast, images extracted at energies above the resonance exhibit a signal that remains substantially localized on the Dy sites. It is noted that the present results will carry over quite generally to $N_{4,5}$ spectroscopic images of other rare-earth elements (except Lu, which does not exhibit resonance). We also anticipate that resonances will give rise to observable effects in $M_{2,3}$ spectroscopic images of the transition-elements.

ation of the transition potentials associated with the Dy-$N_{4,5}$ resonance broadens the appearance of the Dy columns. As the sample thickness increases beyond a few tens of nanometers, the slowly varying transition potentials lead to an approximate preservation of elastic contrast, implying that images extracted from the strong resonance are not directly interpretable. This occurs even when a collection angle significantly larger

* Electronic address: christian.dwyer@monash.edu
[1] U. Fano, Phys. Rev. **124**, 1866 (1961).
[2] A. F. Starance, Phys. Rev. B **5**, 1773 (1972).
[3] J. Sugar, Phys. Rev. B **5**, 1785 (1972).
[4] J. L. Dehmer and A. F. Starance, Phys. Rev. B **5**, 1792 (1972).
[5] N. Dellby, O. L. Krivanek, P. D. Nellist, P. E. Batson, and A. R. Lupini, J. Electr. Microsc. **50**, 177 (2001).

[6] E. Okunishi, H. Sawada, Y. Kondo, and M. Kersker, Microsc. Microanal. **12 (Supp 2)**, 1150 (2006).

[7] M. Bosman, V. J. Keast, J. L. García-Muñoz, A. J. D'Alfonso, S. D. Findlay, and L. J. Allen, Phys. Rev. Lett. **99**, 086102 (2007).

[8] K. Kimoto, T. Asaka, T. Nagai, M. Saito, Y. Matsui, and K. Ishizuka, Nature **450**, 702 (2007).

[9] D. A. Muller, L. F. Kourkoutis, M. Murfitt, J. H. Song, H. Y. Hwang, J. Silcox, N. Dellby, and O. L. Krivanek, Science **319**, 1073 (2008).

[10] D. A. Muller, Nature Materials **8**, 263 (2009).

[11] G. A. Botton, S. Lazar, and C. Dwyer, Ultramicroscopy **110**, 926 (2010).

[12] H. Tan, S. Turner, E. Yücelen, J. Verbeeck, and G. V. Tendeloo, Phys. Rev. Lett. **107**, 107602 (2011).

[13] J. A. Mundy, Q. Mao, C. M. Brooks, D. G. Schlom, and D. A. Muller, Appl. Phys. Lett. **101**, 042907 (2012).

[14] F. Hofer, J. Microsc. **156**, 279 (1989).

[15] C. Zhao, T. Witters, B. Brijs, H. Bender, O. Richard, M. Caymax, T. Heeg, J. Schubert, V. V. Afanas'ev, A. Stesmans, et al., Appl. Phys. Lett. **86**, 132903 (2005).

[16] For simplicity, we have not included the super-Coster-Kronig transitions reported to contribute to the $4d$ absorption spectra of heavier rare-earths [39]. We find that the $4f \rightarrow \epsilon f$ transitions alone provide a sufficient description of the present results.

[17] R. D. Cowan, *Theory of atomic structure and spectra* (University of California Press, 1981).

[18] P. Rez, Microsc. Microanal. **7**, 356 (2001).

[19] Here the splitting of strong transitions is unresolved, so we consider only one discrete level with energy ϵ_d.

[20] G. B. Winkelman, C. Dwyer, T. S. Hudson, D. Nguyen-Manh, M. Döblinger, R. L. Satet, M. J. Hoffmann, andD.J.H. Cockayne, Phil. Mag. Lett. **84**, 755 (2004).

[21] G. B. Winkelman, C. Dwyer, T. S. Hudson, D. Nguyen-Manh, M. Döblinger, R. L. Satet, M. J. Hoffmann, andD.J.H. Cockayne, Appl. Phys. Lett. **87**, 061911 (2005).

[22] H. L. Xin, Y. Zhu, and D. A. Muller, Microsc Microanal. **18**, 720 (2012).

[23] R. F. Loane, P. Xu, and J. Silcox, Acta Cryst. A **47**, 267 (1991).

[24] E. J. Kirkland, *Advanced Computing in Electron Microscopy* (Springer, 2010), 2nd ed., ISBN 1441965327.

[25] J. M. LeBeau, S. D. Findlay, L. J. Allen, and S. Stemmer, Phys. Rev. Lett. **100** (2008).

[26] C. Dwyer, C. Maunders, C. L. Zheng, M. Weyland, P. C. Tiemeijer, andJ. Etheridge, Appl. Phys. Lett. **100**, 191915 (2012).

[27] C. Dwyer, Ultramicroscopy **104**, 141 (2005).

[28] C. Dwyer, Phys. Rev. B **72** (2005).

[29] C. Dwyer, S. D. Findlay, and L. J. Allen, Phys. Rev. B **77** (2008).

[30] R. P. Liferovich and R. H. Mitchell, Journal of Solid State Chemistry **177**, 2188 (2004).

[31] H. Kohl and H. Rose, Adv. Imag. Electr. Phys. **65**, 173 (1985).

[32] D. A. Muller and J. Silcox, Ultramicroscopy **59**, 195 (1995).

[33] L. J. Allen, S. D. Findlay, A. R. Lupini, M. P. Oxley, and S. J. Pennycook, Phys. Rev. Lett. **91**, 105503 (2003).

[34] E. C. Cosgriff, M. P. Oxley, L. J. Allen, and S. J. Pennycook, Ultramicroscopy **102**, 317 (2005).

[35] M. P. Oxley, M. Varela, T. J. Pennycok, K. Van Benthem, S. D. Findlay, A. J. D'Alfonso, L. J. Allen, and S. J. Pennycook, Phys. Rev. B **76**, 064303 (2007).

[36] A. J. D'Alfonso, S. D. Findlay, M. P. Oxley, and L. J. Allen, Ultramicroscopy **108**, 677 (2008).

[37] S. Lazar, Y. Shao, L. Gunawan, R. Nedchache, A. Pignolet, and G. A. Botton, Microsc. Microanal. **16**, 416 (2010).

[38] A. Howie, Proc. Roy. Soc. (Lond.) A **271**, 268 (1963).

[39] H. Ogasawara and A. Kotani, J. Synchrotron Rad. **8**, 220 (2001).